

Article

Ka-Band Miniaturized 90 nm Complementary Metal Oxide Semiconductor Wideband Rat-Race Coupler Using Left-Handed and Right-Handed Transmission Lines

Je-Yao Chang, Tsu-Yu Lo, Pin-Yen Chen, Tan-Zhi Wei, Shih-Ping Huang, Wei-Ting Tsai, Chong-Yi Liou and Shau-Gang Mao * 

Graduate Institute of Commutation Engineering, National Taiwan University, Taipei 106, Taiwan

* Correspondence: sgmao@ntu.edu.tw; Tel.: +886-23366-1576

Abstract: The traditional rat-race coupler comprises a quarter-wavelength transmission line and a three-quarter-wavelength transmission line. In this design, the slow-wave structure transmission line is employed to replace the conventional quarter-wavelength transmission line, and the three-quarter-wavelength transmission line is substituted with the left-handed transmission line. By using the TSMC CMOS 90 nm fabrication process, a circuit is created with a chip size of $300\ \mu\text{m} \times 200\ \mu\text{m}$, corresponding to the electrical size at 39 GHz of $0.039\lambda_0 \times 0.026\lambda_0$. The measured results demonstrate that the operating bandwidth is 35 to 43 GHz, with an amplitude imbalance of around 0 dB, a phase error within 1° , a return loss of less than 26 dB, and an isolation better than 40 dB.

Keywords: metamaterial; composite right/left-handed transmission line; rat-race coupler; slow wave



Citation: Chang, J.-Y.; Lo, T.-Y.; Chen, P.-Y.; Wei, T.-Z.; Huang, S.-P.; Tsai, W.-T.; Liou, C.-Y.; Mao, S.-G. Ka-Band Miniaturized 90 nm Complementary Metal Oxide Semiconductor Wideband Rat-Race Coupler Using Left-Handed and Right-Handed Transmission Lines. *Electronics* **2024**, *13*, 417. <https://doi.org/10.3390/electronics13020417>

Academic Editor: Filippo Costa

Received: 18 December 2023

Revised: 14 January 2024

Accepted: 17 January 2024

Published: 19 January 2024



Copyright: © 2024 by the authors. Licensee MDPI, Basel, Switzerland. This article is an open access article distributed under the terms and conditions of the Creative Commons Attribution (CC BY) license (<https://creativecommons.org/licenses/by/4.0/>).

1. Introduction

Electromagnetic metamaterials are extensively employed across diverse domains. Within the optics field, the implementation of superlenses exhibiting negative refractive indices is facilitated extensively, thereby enabling super-resolution imaging capabilities [1,2]. Furthermore, these artificial metamaterials find practical applications in optical microscopes and imaging systems [3,4].

In the domain of RF and microwave technology, electromagnetic metamaterials play a crucial role in the design of antennas [5–10] and filters [11–16]. By leveraging the novel characteristics of these materials, antennas can achieve size reduction and gain and directivity enhancement. Similarly, electromagnetic metamaterials facilitate the stringent properties of signal transmission and reflection within specific frequency ranges, rendering them highly suitable for filter design.

Moreover, the negative refractive characteristics of electromagnetic metamaterials can be effectively utilized in RF invisibility technology [17–20], enabling the transparency of objects from visible light to radio frequency. This capability creates opportunities for concealing or mitigating interference arising from RF signals.

This paper focuses on the RF circuit design application of electromagnetic metamaterials to create a compact 90 nm CMOS wideband rat-race coupler while maintaining optimal performance.

When designing a rat-race coupler, several crucial factors are considered, including impedance matching, phase imbalance, and loss imbalance across the operating bandwidth. The conventional rat-race coupler consists of three -90° quarter-wavelength transmission lines and one -270° three-quarter-wavelength transmission line, as depicted in Figure 1a.

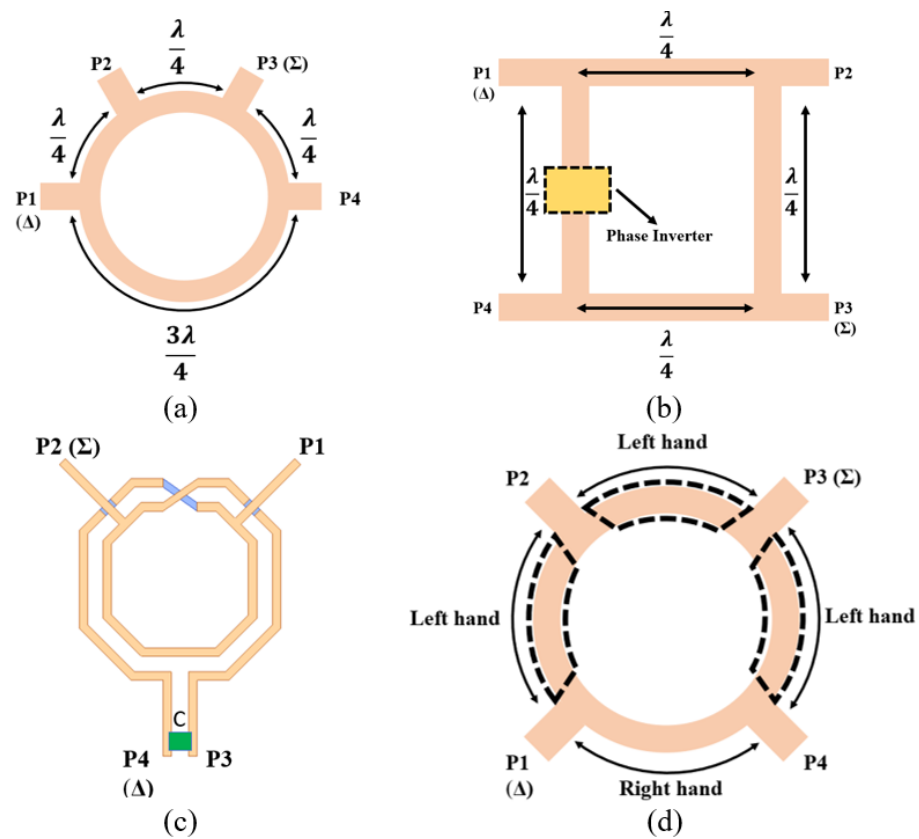


Figure 1. (a) Traditional rat-race coupler, (b) simplified view of ring hybrid with phase inverter, (c) equivalent circuit of a folded inductor rat-race coupler, (d) left-hand and right-hand rat-race coupler.

However, this configuration brings undesirable properties. First, the loss is imbalanced in the differential outputs, which is because one path passes through a -90° transmission line, while the other path passes through a -270° transmission line. Second, the variation in phase difference between the differential outputs is remarkable with different frequencies, following a linear equation of $\varphi_{\text{diffT}} = \frac{\omega}{\omega_0} \cdot \pi$. Consequently, the bandwidth is restricted to a narrow range especially when a phase error requirement is stringent, for example, a 5° phase difference. Third, the size of the rat-race coupler is determined by the transmission line lengths.

Hence, the conventional quarter-wavelength transmission line is usually quite large with respect to the allowable area, making it difficult to accommodate it within the available semiconductor chip fabrication. To address these challenges, alternative architectures have been proposed. Figure 1b shows circuits presented in [21–24], where meander lines and multi-layer microstrip lines are employed to significantly reduce the length of the quarter-wavelength transmission lines. Moreover, the phase inverter is adopted to achieve the required -270° transmission lines. Although this approach achieves a compact circuit size, it may introduce substantial loss imbalance. Figure 1c represents the architecture introduced in [25,26], which uses folded inductors to simulate the necessary transmission structure for the rat-race coupler through inductor coupling. However, variations in the manufacturing process of the inductors can lead to significant differences between the simulated and measured results. In [27], bridged T-coils are used to replace the transmission line section in conventional passive circuit designs, thereby reducing the circuit size substantially without reducing the operating bandwidth. However, the architecture of this circuit employs a traditional rat-race coupler comprising bridged T-coil structures of varying lengths. As a result, it still encounters issues such as limited bandwidth and imbalanced losses.

In the proposed design, a compact rat-race coupler is introduced, employing both a composite right/left-handed transmission line (CRLH) and a right-handed slow-wave

transmission line, with a center frequency set at 39 GHz, as depicted in Figure 1d. The CRLH structure enables the achievement of distinct electromagnetic metamaterial properties via the integration of forward propagation (right hand, RH) and backward propagation (left hand, LH) characteristics. This integration allows for the generation of advanced phases and negative group velocities within a specified frequency range. The slow-wave transmission lines have right-handed characteristics and are designed to keep the electromagnetic wave group velocity below the speed of light in a substrate to achieve signal delay and thereby reduce the size of the transmission line.

The proposed design possesses several advantages. Firstly, it results in low loss imbalance as the signals from P1 to P2 and P4 pass through quarter-wavelength transmission lines, ensuring similar losses in both paths. Additionally, the phase difference between the CRLH and right-handed slow-wave transmission lines forms a curve with a minimum value, thereby achieving the minimum phase imbalance. By designing this curve to have zero slope near the desired center frequency, the overall phase bandwidth can be enhanced.

Furthermore, the use of the $+90^\circ$ phase angle CRLH, created by series capacitors and parallel inductors, along with their inherent parasitic inductance and capacitance, significantly reduces the length of the transmission line. This is achieved by reducing the number of stages. The right-handed slow-wave transmission line contributes to the design by forming the -90° phase transmission line, enabling further size reduction.

An additional benefit of this design is its low sensitivity to process variations. By using CRLH to eliminate the need for an inductor coupling mechanism, the design minimizes the impact of process variations and packaging effects.

Overall, this approach not only overcomes size limitations but also offers improved performance in rat-race coupler designs. It provides a compact solution that addresses challenges related to size constraints, loss and phase imbalances, and process variations.

The structure of this article is as follows: Section 2 carries out a theoretical analysis and simulation design and is divided into three parts for explanation. The first part of Section 2 is the design of left-handed transmission lines, which includes the theoretical analysis, formula derivation, and simulation results of left-handed transmission lines. The second part of Section 2 is the design of right-handed transmission lines, which includes the theoretical analysis, formula derivation, and simulation results of right-handed slow-wave transmission lines. The third part of the second section integrates the results of the first two parts to form a left-handed and right-handed rat-race coupler and presents the simulation results. Section 3 presents the actual measurement results, comparisons with simulation results, and finally comparisons with similar research results. Section 4 provides some conclusions.

2. Theoretical Analysis and Simulation Results

2.1. Left-Handed Transmission Line Design

The left-handed (LH) characteristic of this structure dominates the phase and amplitude responses. The left-handed transmission line is first considered. Considering that the area required to implement inductors in 90 nm CMOS technology provided by TSMC is much larger than that for capacitors, we decided to use a T-model symmetric structure in the implementation of the unit cell for the left-handed transmission line, where the series capacitors are cascaded with parallel inductors and then cascaded with series capacitors, shown in Figure 2.

The characteristic impedance and S_{21} of this structure can be calculated using the ABCD Matrix from the T-model.

$$Z_c = \sqrt{\frac{L_L}{C_L \left(1 - \frac{1}{4\omega^2 L_L C_L}\right)}} \quad (1)$$

$$S_{21} = \frac{1}{\left(1 - \frac{1}{2\omega^2 L_L C_L}\right) - j\left(\frac{1}{\omega\sqrt{L_L C_L}} \sqrt{1 - \frac{1}{4\omega^2 L_L C_L}}\right)} \quad (2)$$

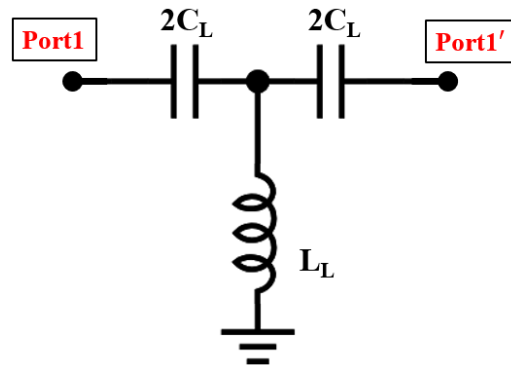


Figure 2. LH equivalent T-model.

In order to create a 1/4-wavelength transmission line with an impedance of $Z_c = 70.7 \Omega$ that can be used in the frequency band, it is necessary to calculate the required capacitance and inductance values to obtain the required minimum order. The phase of the left-hand transmission line can be derived using the ABCD Matrix from the T-model and transformation to an S-parameter and can be written as [28]

$$\varnothing_L = N \cdot \varnothing_{S_{21}} = N \cdot \arctan \left(\frac{\left(1 - \frac{1}{4}(\omega\sqrt{L_L C_L})^{-2}\right)^{0.5}}{\omega\sqrt{(L_L C_L)} \left(1 - \frac{1}{2}(\omega\sqrt{L_L C_L})^{-2}\right)} \right) \quad (3)$$

Here, \varnothing_L represents the phase of the transmission line, N denotes the order of the T-model, L_L indicates the shunt inductance, and C_L represents the series capacitance. From Equation (3), it can be observed that to minimize the area, only one unit cell ($N = 1$) is needed to achieve a $+90^\circ$ phase shift at the center frequency f_0 . In this case, the value inside the arctan function should approach infinity, which means $\frac{1}{2}(\omega_0\sqrt{L_L C_L})^{-2} = 1$, and $\omega_0 = 2\pi f_0$.

Then

$$\sqrt{L_L C_L} = \frac{1}{\omega_0\sqrt{2}} \quad (4)$$

and the cutoff frequency of the unit cell in Figure 2 is written as

$$f_c = \frac{1}{4\pi\sqrt{L_L C_L}} \quad (5)$$

The cutoff frequency $f_c = \frac{\omega_0\sqrt{2}}{4\pi}$ is calculated to be 27.6 GHz for a center frequency of 39 GHz in this design. Additionally, as the number of stages increases, for instance, when $N = 2$ as described in Equation (3), the cutoff frequency decreases to 15 GHz, which indicates a broader operating bandwidth. However, this also results in an increased number of components, leading to a larger area. Therefore, $N = 1$ offers a satisfactory bandwidth, making it suitable for the design and enabling the construction of a compact structure.

The values of inductance and capacitance required for a pure left-handed transmission line composed of only one T-model can be calculated by solving the simultaneous equations

in Equations (1) and (3). For a desired phase requirement of $+90^\circ$ at a center frequency of 39 GHz and a characteristic impedance of 70.7Ω , the following values can be obtained.

$$\begin{cases} Z_c = \sqrt{\frac{L_L}{C_L} \left(1 - \frac{1}{4\omega^2 L_L C_L}\right)} = 70.7 \\ \sqrt{L_L C_L} = \frac{1}{\omega_0 \sqrt{2}} \end{cases} \quad (6)$$

$$L_L = 288\text{pH}, C_L = 0.0288\text{pF}$$

The created left-handed transmission line possesses the parasitic characteristics of the right-handed transmission line, causing a reduction in phase lead. Therefore, a composite left-handed and right-handed transmission line is proposed in the actual design.

It is crucial to consider the parasitic elements in a $1/4$ -wavelength CRLH transmission line, L_P and C_P . Thus, the actual equivalent circuit model can be represented as shown in Figure 3. The values of L_P and C_P are highly dependent on the layout of the circuit. L_P arises from the inductance caused by the interconnecting lines between passive components, while C_P is due to the capacitance between all components and the ground plane, R_L is metal loss, and G_L is substrate loss.

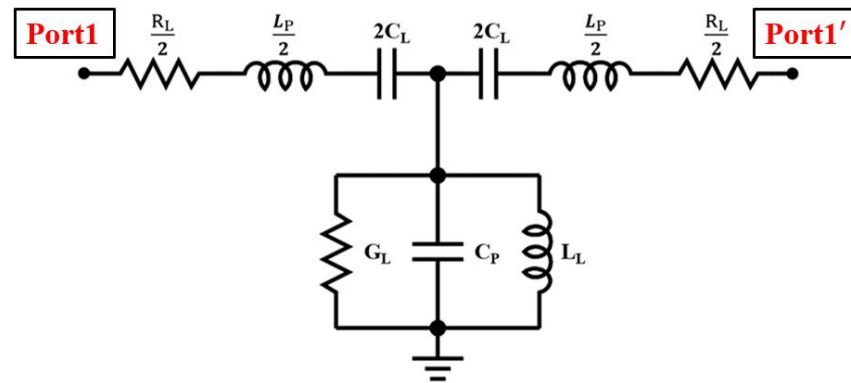


Figure 3. CRLH equivalent circuit T-model.

The parasitic inductance and capacitance are generally very small, so the resulting phase can be simplified as $\phi_p = -\omega \sqrt{L_P C_P}$ [28]. And the actual phase of the left-handed transmission line is

$$\phi_{\text{CRLH}} = \arctan\left(\frac{\left(1 - \frac{1}{4}(\omega \sqrt{L_L C_L})^{-2}\right)^{0.5}}{\omega \sqrt{L_L C_L} \left(1 - \frac{1}{2}(\omega \sqrt{L_L C_L})^{-2}\right)}\right) - \omega \sqrt{L_P C_P} \quad (7)$$

In Equation (7), L_P and C_P represent the parasitic inductance capacitance, respectively. The parasitic right-handed circuits would cause a reduction in the leading phase magnitude formed by the left-handed line. The values of inductance and capacitance of the left-handed transmission line need to be reduced to maintain the desired $+90^\circ$ phase at the center frequency. Utilizing these parasitic right-hand circuits appears to reduce the capacitance and inductance values required for the left-hand transmission line. According to Equation (5), if the capacitance and inductance required for the left-hand transmission line are reduced, the cutoff frequency of the circuit is increased, and the increase in the cutoff frequency leads to a reduction in bandwidth. Although the circuit area is decreased, an increase in cutoff frequency results in a reduction in bandwidth.

The final fine-tuned values obtained from this process are $L_L = 260 \text{ pH}$, $C_L = 0.025 \text{ pF}$, $L_P = 88 \text{ pH}$, $C_P = 5.5 \text{ fF}$, $R_L = 7.6 \Omega$, and $G_L = 700 \Omega$. The full-wave simulation model is shown in Figure 4, while the extracted values agree well with the results of the 3D full-wave simulation, as shown in Figure 5a,b. Moreover, the phase is close to $+90^\circ$ at the

center frequency of 39 GHz. The equivalent μ and ϵ of the left-handed quarter-wavelength transmission line can be calculated through the formula [29].

$$\mu_{\text{eff}} = \mu'_{\text{eff}} - j\mu''_{\text{eff}} = \pm \left(\frac{1 + \Gamma}{1 - \Gamma} \right) \frac{Z_a^{\text{TL}}}{Z_a^{\text{TL}}} \frac{1}{jL} \left(\frac{c}{\omega} \right) \cosh^{-1} \left(\frac{1 - S_{11}^2 + S_{21}^2}{2S_{21}} \right). \quad (8)$$

$$\epsilon_{\text{eff}} = \epsilon'_{\text{eff}} - j\epsilon''_{\text{eff}} = \pm \left(\frac{1 - \Gamma}{1 + \Gamma} \right) \frac{Z_a^{\text{TL}}}{Z_a^{\text{TL}}} \frac{1}{jL} \left(\frac{c}{\omega} \right) \cosh^{-1} \left(\frac{1 - S_{11}^2 + S_{21}^2}{2S_{21}} \right). \quad (9)$$

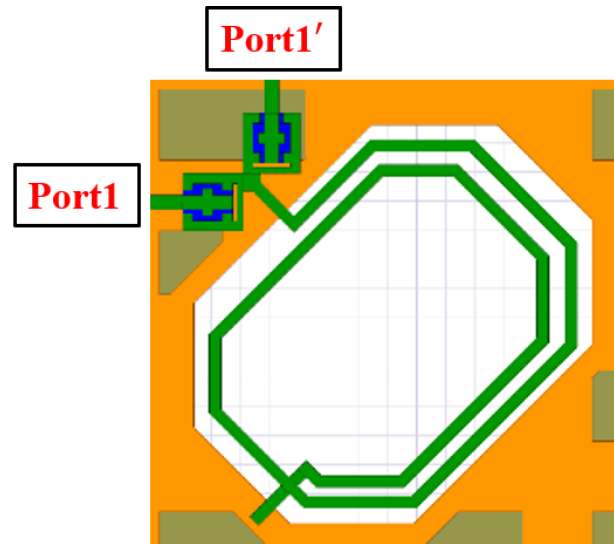


Figure 4. CRLH 3D simulation model.

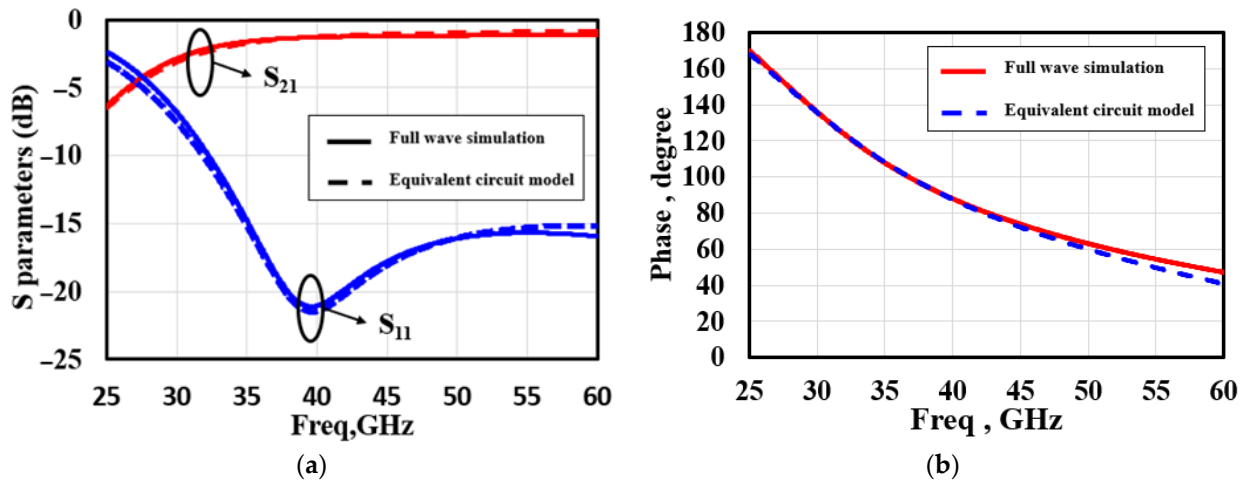


Figure 5. (a) S-parameter of the two models. (b) Phase of the two models.

As shown in Figure 6, it can be seen that μ'_{eff} and ϵ'_{eff} are -40 and -15 at 39 GHz, respectively. The negative values confirm that the structure under consideration is a left-handed transmission line. Furthermore, these values are considerably higher than the ϵ_r ($\cong 3.8$) of the CMOS process, resulting in a substantial reduction in the effective wavelength ($\lambda_g = \frac{2\pi}{|\beta|} = \frac{2\pi}{\omega\sqrt{|\mu\epsilon|}}$) [30]. Additionally, μ''_{eff} and ϵ''_{eff} are both close to zero, indicating a low-loss structure. Compared to a traditional transmission line, the length of the CRLH transmission line is significantly shortened to $80 \mu\text{m}$, which is about 8% of the length of a conventional transmission line.

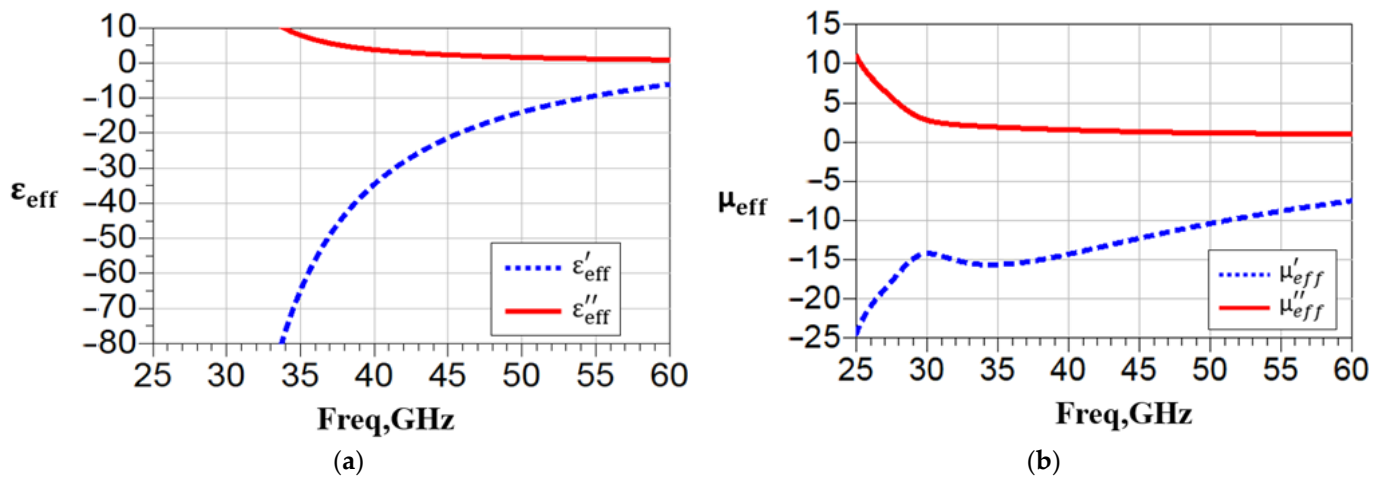


Figure 6. Simulation of left-handed transmission lines (a) ϵ_{eff} and (b) μ_{eff} .

2.2. Right-Handed Transmission Line Design

When designing the transmission line for the right-handed (RH) component, the parasitic circuit of each stage follows the same form as the inherent right-handed transmission line, consisting of series inductors and parallel capacitors. Therefore, there is no need to restrict the design to a single stage. Multi-stage transmission lines have very small capacitance and inductance values. Therefore, the calculated cutoff frequency will be much higher than the center frequency. Thus, the phase calculation formula can be simplified as [28]

$$\varnothing_R = -N_2 \left(\omega \sqrt{L_R C_R} \right) \quad (10)$$

\varnothing_R represents the phase of the transmission line, N_2 represents the order of the right-handed transmission line model, L_R represents the series inductance, and C_R represents the shunt capacitance.

The right-handed slow-wave transmission line is achieved through a series of multi-order inductors and parallel capacitors, as shown in Figure 7a. In order to consider a circuit with a compact size and symmetry, this periodic structure is connected by a transmission line (T_L), allowing it to be folded and thus reducing the overall space required. This structure can be simplified as two right-handed structures (RH1 and RH2) connected together; each structure is formed by 11 series of serial inductors and parallel capacitors, as shown in Figure 7b. The values of the extracted inductance and capacitance are $L_R = 21.5$ pH and $C_R = 4.45$ fF, respectively. The resistance R_R is 0.2Ω , and the conductance G_R is 6000Ω .

The comparison between the S-parameters and the phase of the extracted equivalent circuit and the full-wave simulation is shown in Figure 8a,b. A good agreement is obtained, and the phase is close to -90° at the center frequency of 39 GHz.

Similarly, the equivalent μ and ϵ of the right-handed slow-wave transmission line can be calculated by Equations (8) and (9), as shown in Figure 9. ϵ'_{eff} and μ'_{eff} are approximately 18 and 8, respectively. The positive values indicate that this transmission line possesses the right-handed characteristic, and the values are much larger than the substrate permittivity $\epsilon_r = 12.9$, ensuring that the group velocity of this structure is significantly less than the speed of light in free space and thus demonstrating a good slow-wave effect. Additionally, μ''_{eff} and ϵ''_{eff} are 1.5 and 0.5, respectively, indicating a low-loss structure. Furthermore, the length of this transmission line is only about 30% of the traditional transmission line.

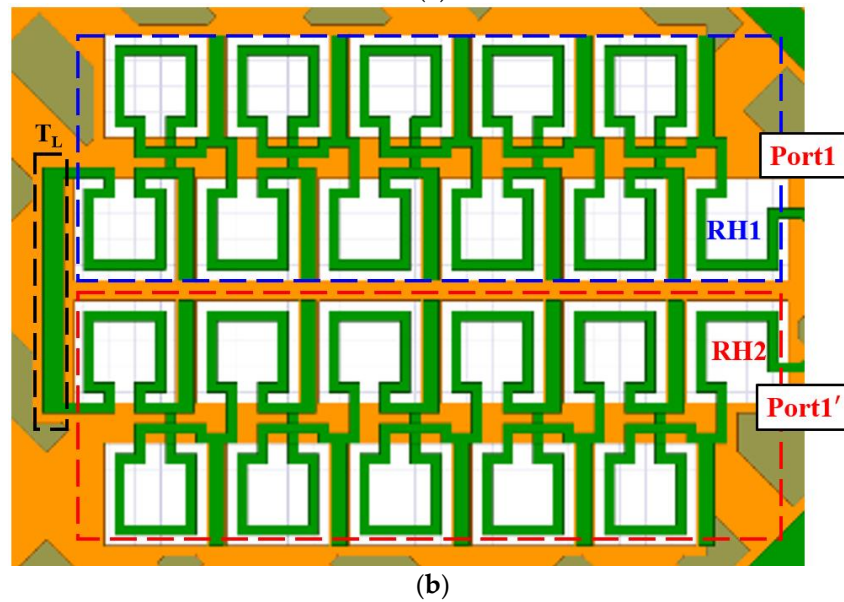
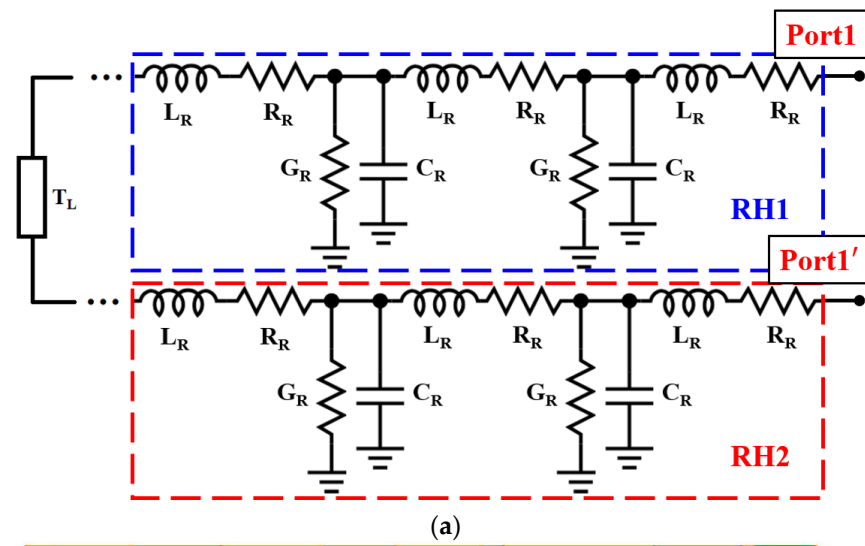


Figure 7. (a) Slow-wave equivalent circuit model. (b) Slow-wave 3D simulation model.

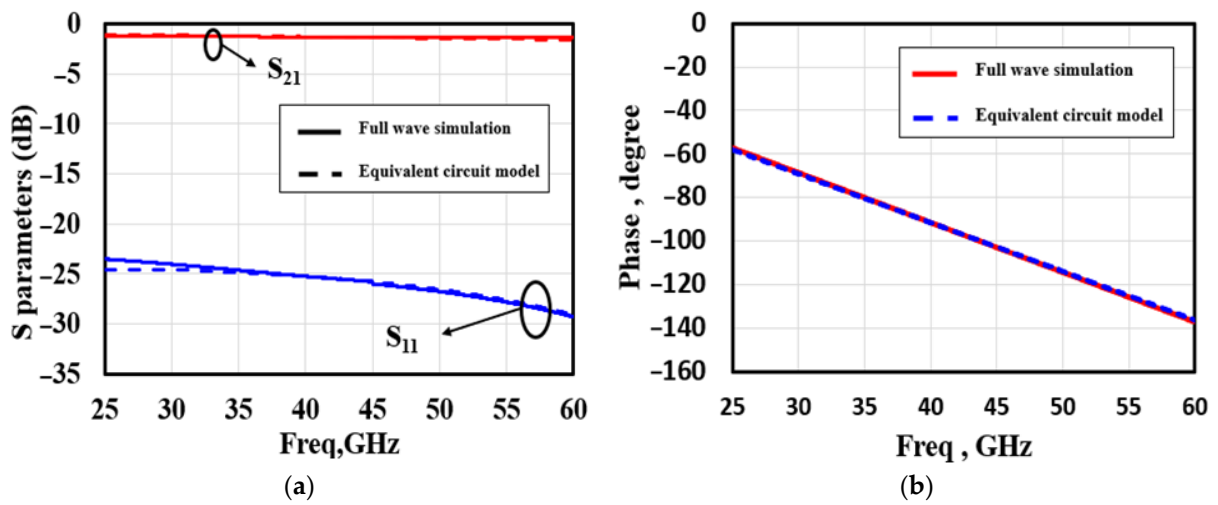


Figure 8. (a) S-parameter of the two models. (b) Phase of the two models.

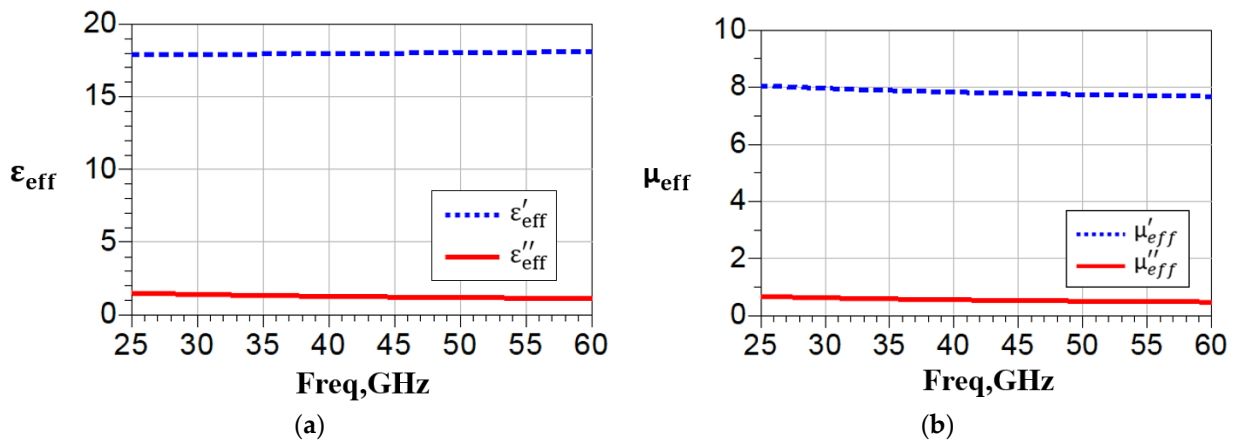


Figure 9. Simulation of right-handed slow-wave transmission lines (a) ϵ_{eff} and (b) μ_{eff} .

2.3. Left-Handed and Right-Handed Rat-Race Coupler

By combining the three designed CRLHs ($+90^\circ$) and one right-handed slow-wave transmission line (-90°) shown in Figure 10, the left-handed and right-handed rat-race coupler is proposed. The ground is constructed using two bottom metal layers in an alternating slot pattern to comply with the metal density rule of TSMC CMOS 90 nm technology.

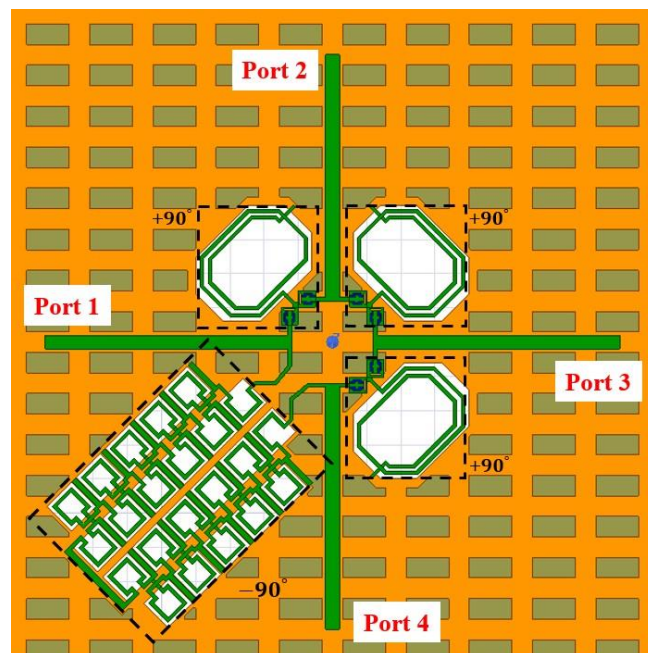


Figure 10. Full-wave simulation circuit.

For traditional rat-race couplers, the frequency-dependent phase difference between the differential outputs can be expressed as $\phi_{diffT} = \frac{\omega}{\omega_0} \pi$. In the design of the left-handed and right-handed rat-race coupler, the phase difference is given by

$$\phi_{diff} = \phi_{CRLH} - \phi_{slowwave} = \arctan \left(\frac{\left(1 - \frac{1}{4}(\omega\sqrt{L_L C_L})^{-2}\right)^{0.5}}{\omega\sqrt{L_L C_L} \left(1 - \frac{1}{2}(\omega\sqrt{L_L C_L})^{-2}\right)} \right) + N_2 \left(\omega\sqrt{L_R C_R} \right) - \omega\sqrt{L_P C_P} \quad (11)$$

It can be observed that $\varnothing_{\text{diff}}$ in the proposed CRLH coupler exhibits a parabolical frequency response compared to the traditional structure with linear response shown in Figure 11, indicating that the operating bandwidth of the presented structure is significantly extended.

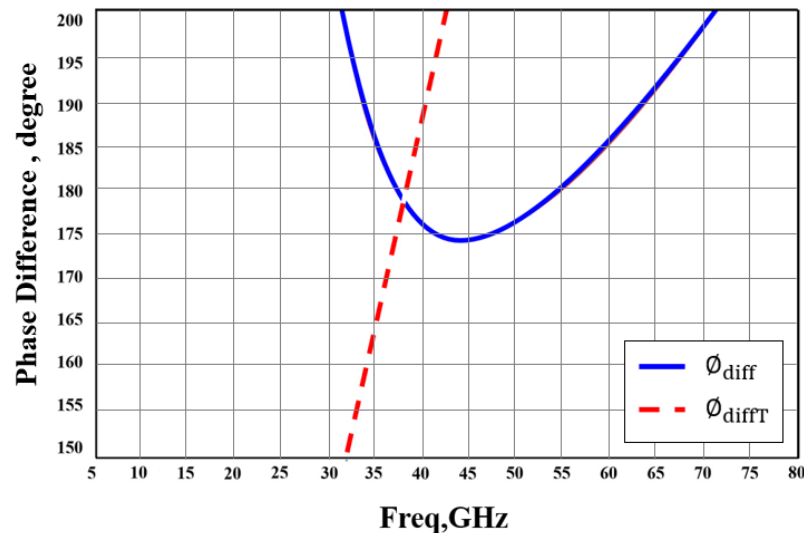


Figure 11. Phase difference of traditional rat-race coupler and left-handed and right-handed rat-race coupler.

3. Implementation and Measurement Results

To validate the usefulness of the CRLH structure design, the miniaturized rat-race coupler is implemented by using a 90 nm CMOS process at a center frequency of 39 GHz to achieve good matching, phase balance, and low-loss imbalance over a wide bandwidth. The CRLH transmission line is created as a one-stage T-model structure with a Metal–Insulator–Metal (MIM) capacitor and a coiled inductor without underlying metal ground.

For the right-handed slow-wave transmission line design, a multi-stage slow-wave structure is created by combining the square-shaped inductors with short stub structures that provide sufficient capacitance. This arrangement enables a compact arrangement of periodic patterns, thereby reducing the overall layout area of the transmission line. In order to reduce the overall area more effectively, it is designed as a bent slow-wave transmission line. The chip photo of the four-port rat-race coupler is depicted in Figure 12, featuring a core circuit area of $200 \mu\text{m} \times 300 \mu\text{m}$.

Figure 13 shows the measurement results of return loss and isolation. Since the proposed rat-race coupler is symmetrical in design, the return losses for port 1 and port 4 are the same, and the return losses for port 2 and port 3 are the same, so only the return losses of port 1 and port 2 are shown in Figure 13. By analyzing the return loss measurement results, it can be seen that S_{11} and S_{22} are both less than -15 dB in the frequency range from 35 GHz to 43 GHz. S_{24} represents the isolation of the proposed rat-race coupler; it can be seen from Figure 13 that the isolation is greater than 25 dB in the frequency range from 35 GHz to 43 GHz.

The proposed rat-race coupler can be used in two modes: differential mode and common mode, so Figure 14 shows the insertion loss of the two modes. Port 1 is the differential mode input, and port 2 and port 4 are the differential mode output, so S_{21} and S_{41} represent the insertion loss of the differential mode. Port 3 is the common mode input, and port 2 and port 4 are the common mode output, so S_{23} and S_{43} represent the common mode insertion loss. Since the proposed rat-race coupler is symmetrical in design, S_{21} and S_{43} are the same, so Figure 14 only shows three curves S_{21} , S_{41} , and S_{23} . In Figure 14, the insertion loss of the three curves S_{21} , S_{23} , and S_{41} at 39 GHz is about 4.4 dB, and the loss variation is within 1 dB in the frequency range of 36 GHz to 48 GHz.

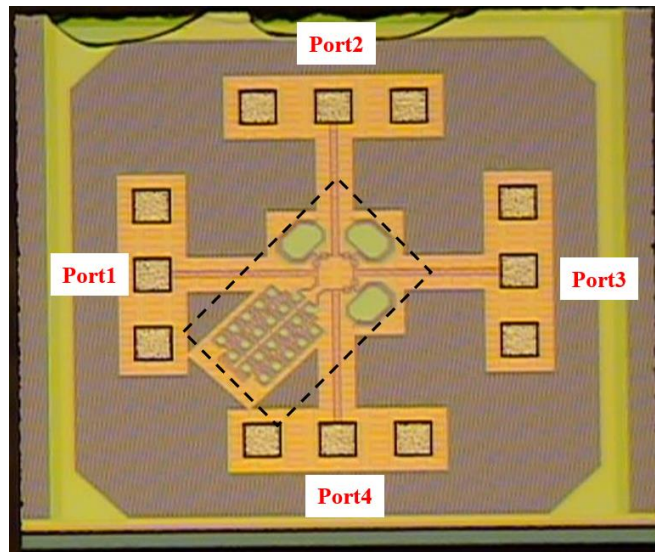


Figure 12. Microscopic image of the rat-race chip (DIE SIZE: 700 μm × 700 μm, core circuit in dash line: 200 μm × 300 μm).

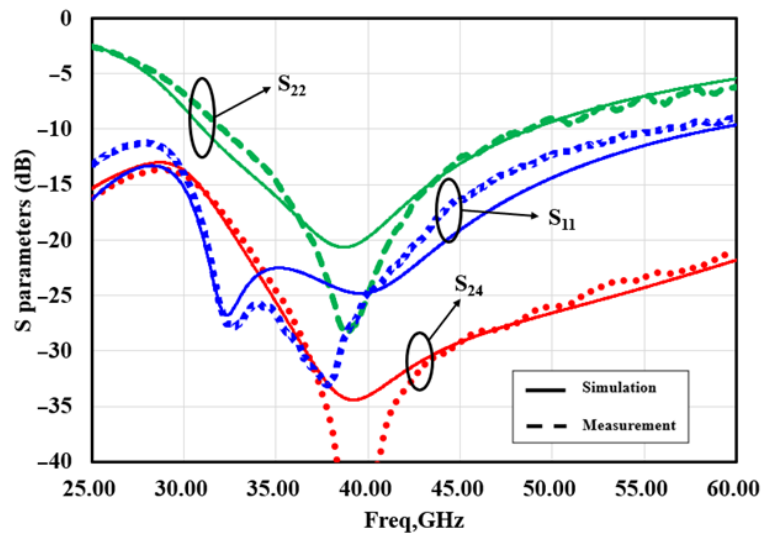


Figure 13. Return loss and isolation.

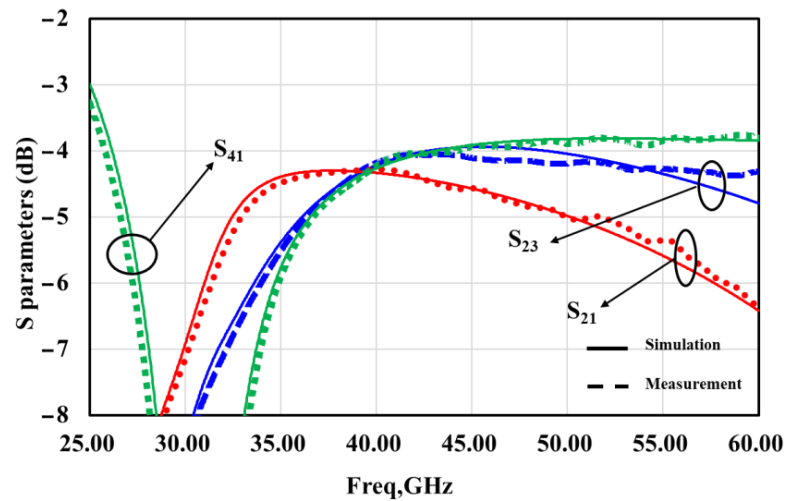


Figure 14. Insertion loss.

Figure 15 shows the phase difference for the differential port and common port, with targets of 180° and 0°, respectively. In the frequency range of 32 GHz to 60 GHz, the differential port phase error is maintained within the range of plus or minus 5° of 180°. In the frequency range of 34 GHz to 60 GHz, the common port phase error is maintained within the range of plus or minus 5° of 0°.

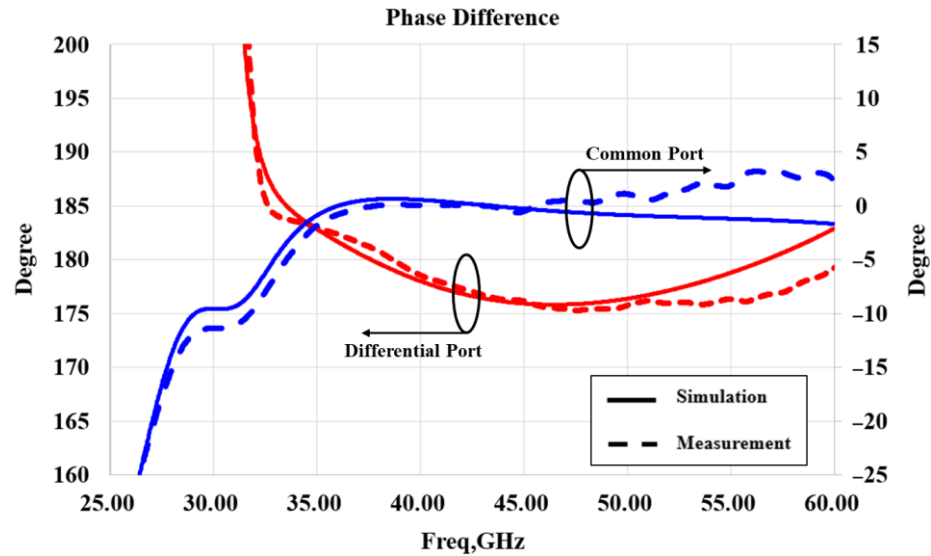


Figure 15. Differential port and common port phase difference.

Table 1 shows the performance comparison of the proposed CRLH rat-race coupler with other millimeter-wave rat-race coupler designs. The data in the table are differential mode measurement results.

Table 1. Performance summary and comparison among the state-of-the-art integrated couplers.

Process	Center Frequency (f_c)/ Fractional Bandwidth	Coupled IL@ f_c	Through IL@ f_c	Isolation Isolation@ f_c	Return Loss @ f_c	Phase Error @ f_c	Amplitude Error @ f_c	Electrical Size
[21]	130 nm SiGe BiCMOS 60 GHz/*	4.1 dB	5.7 dB	21 dB	18 dB	4°	~1.6 dB	0.00446 λ_0^2
[22]	130 nm BiCMOS 60 GHz/10%	6 dB	6 dB	27 dB	26 dB	5°	~0 dB	0.01102 λ_0^2
[23]	250 nm CMOS 30 GHz/*	3.1 dB	5.7 dB	17 dB	18 dB	< 5°	~2.6 dB	0.00086 λ_0^2
[24]	GaAs 45 nm SOI CMOS 43 GHz/17%	5 dB	5 dB	28 dB	20 dB	5°	~0 dB	0.0263 λ_0^2
[25]	130 nm CMOS 33 GHz/**	5.3 dB	5.4 dB	22 dB	10.5dB	3°	~0.1 dB	0.00292 λ_0^2
[26]	130 nm CMOS 70 GHz/15.7%	4.1 dB	4.1 dB	20 dB	16.2 dB	< 3°	~0 dB	0.00203 λ_0^2
[27]	180 nm CMOS 60 GHz/9.8%	7.07 dB	6.04 dB	28 dB	18.4dB	3°	1 dB	0.00292 λ_0^2
This work	90 nm CMOS 39 GHz/19.4%	4.4 dB	4.4 dB	40 dB	26 dB	< 1°	~0 dB	0.00101 λ_0^2

All results correspond to the case with the input at Δ - port. Fractional bandwidth defined under a phase error < 5° and input return loss > 15 dB and amplitude error < 1 dB. *: Amplitude error > 1 dB **: return loss < 15 dB.

To make a consistent comparison of different designs, the calculation of fractional bandwidth follows some conditions under phase error < 5 degrees, return loss > 15 dB, and amplitude error < 1 dB. In addition to the comparison of electrical characteristics, the usage area is also a very important indicator. Moreover, to make the area comparison fair, the chip area is divided by the wavelength of the central operating frequency. Therefore, by analyzing these two parameters, it can be concluded that the proposed CRLH rat-race coupler possesses the optimal performance.

Since the amplitude error in [21,23] is greater than 1 dB, and the return loss in [25] is <15 dB, these three designs do not have fractional bandwidth. By comparing the fractional bandwidths, the proposed CRLH rat-race coupler has the widest bandwidth. In addition to the comparison of electrical characteristics, the size of the core circuit is also a very important indicator. To make the size comparison fair, the size of the core circuit is divided by the wavelength of the central frequency. It can be seen from Table 1 that the proposed CRLH rat-race coupler has the second smallest area, second only to [23], but the amplitude error of [23] is also the largest in the comparison table. Therefore, considering the two factors of fractional bandwidth and chip area, the proposed CRLH rat-race coupler has the best performance.

4. Conclusions

Theoretical and experimental studies were conducted on the rat-race coupler consisting of CRLH and RH transmission structures. The circuit was manufactured using TSMC CMOS 90 nm process, the operating frequency is 35 to 43 GHz, and the core circuit size is $300 \mu\text{m} \times 200 \mu\text{m}$, corresponding to the electrical size of $0.039\lambda_0 \times 0.026\lambda_0$. Measurement results show that the CRLH rat-race coupler achieves an amplitude error < 1 dB, phase error < 5° , return loss > 15 dB, and isolation > 25 dB in the frequency range from 35 to 43 GHz. Through the comparison table, the proposed CRLH rat-race coupler has the best fractional bandwidth and achieves excellent results in area reduction. Measurement results and comparisons with different designs demonstrate the effectiveness of the CRLH and RH transmission structures, which feature a wide bandwidth, low loss, good port imbalance, and compact size.

Author Contributions: Conceptualization, S.-G.M.; data curation; methodology, T.-Z.W., W.-T.T. and C.-Y.L.; visualization, P.-Y.C. and S.-P.H.; supervision, S.-G.M.; writing—original draft, T.-Y.L. and J.-Y.C. All authors have read and agreed to the published version of the manuscript.

Funding: This research was financially supported by the Ministry of Science and Technology, Taiwan. Grant ID: NSTC 112-2221-E-002-171.

Data Availability Statement: The data are not publicly available due to privacy concerns. The data presented in this study are available on request from the corresponding author.

Conflicts of Interest: The authors declare no conflicts of interest.

References

1. Eccleston, K.W.; Platt, I.G.; Tan, A.E.-C.; Woodhead, I.M. Fully-printed S-band SRR/wire NRI lens with reduced wire density. In Proceedings of the 2017 Sixth Asia-Pacific Conf. Antennas Propagation, Xi'an, China, 16–19 October 2017; p. 3.
2. Eccleston, K.W.; Zhou, Y.; Platt, I.G.; Tan, A.E.-C.; Woodhead, I.M. Modelling of the Dielectric Resonator and Metal Strip Based Negative-Refractive-Index Lens. In Proceedings of the 2021 IEEE Asia-Pacific Microw Conference, Brisbane, Australia, 28 November–1 December 2021; pp. 253–255.
3. Eccleston, K.W.; Zhou, Y.; Platt, I.G.; Tan, A.E.-C.; Woodhead, I.M. Demonstration of a Negative-Refractive-Index Lens Imaging System. In Proceedings of the 2022 Asia-Pacific Microw Conference (APMC), Yokohama, Japan, 29 November–2 December 2022; pp. 901–903.
4. Eccleston, K.W.; Zhou, Y.; Platt, I.G.; Tan, A.E.-C.; Anton, E.; Woodhead, I.M. Multipixel Metamaterial Lens Imaging System. In Proceedings of the 2022 IEEE Conf. Antenna Measurements Applications (CAMA), Guangzhou, China, 14–17 November 2022; pp. 1–3.
5. Ren, J.; Gong, S.; Jiang, W. Low-RCS monopolar patch antenna based on a dual-ring metamaterial absorber. *IEEE Antennas Wirel. Propag. Lett.* **2018**, *17*, 102–105. [[CrossRef](#)]
6. Shi, X.; Cao, Y.; Hu, Y.; Luo, X.; Yang, H.; Ye, L.H. A high-gain antipodal Vivaldi antenna with director and metamaterial at 1–28 GHz. *IEEE Antennas Wirel. Propag. Lett.* **2021**, *20*, 2432–2436. [[CrossRef](#)]
7. Sun, K.; Han, S.; Choi, J.H.; Lee, J.K. Miniaturized active metamaterial resonant antenna with improved radiation performance based on negative-resistance-enhanced CRLH transmission lines. *IEEE Antennas Wirel. Propag. Lett.* **2018**, *17*, 1162–1165. [[CrossRef](#)]
8. Jia, D.; He, Y.; Ding, N.; Zhou, J.; Du, B.; Zhang, W. Beam-steering flat lens antenna based on multilayer gradient index metamaterials. *IEEE Antennas Wirel. Propag. Lett.* **2018**, *17*, 1510–1514. [[CrossRef](#)]

9. Wang, Z.; Dong, Y. Metamaterial-based vertically polarized miniaturized beam-steering antenna for reconfigurable sub-6 GHz applications. *IEEE Antennas Wirel. Propag. Lett.* **2022**, *21*, 2239–2243. [[CrossRef](#)]
10. Zhao, M.; Zhu, S.; Huang, H.; Hu, D.; Chen, X.; Chen, J.; Zhang, A. Frequency-diverse metamaterial cavity antenna for microwave coincidence imaging. *IEEE Antennas Wirel. Propag. Lett.* **2021**, *20*, 1103–1107. [[CrossRef](#)]
11. Qiao, Z.; Pan, X.; Zhang, F.; Xu, J. A tunable dual-band metamaterial filter based on the coupling between two crossed SRRs. *IEEE Photonics J.* **2021**, *13*, 4600207. [[CrossRef](#)]
12. Hu, F.; Wang, H.; Zhang, X.; Xu, X.; Jiang, W.; Rong, Q.; Zhao, S.; Jiang, M.; Zhang, W.; Han, J. Electrically Triggered Tunable Terahertz Band-Pass Filter Based on VO₂ Hybrid Metamaterial. *IEEE J. Sel. Top. Quantum Electron* **2019**, *25*, 4700207. [[CrossRef](#)]
13. Brown, J.A.; Barth, S.; Smyth, B.P.; Iyer, A.K. Compact mechanically tunable microstrip bandstop filter with constant absolute bandwidth using an embedded metamaterial-based EBG. *IEEE Trans. Microw. Theory Tech.* **2020**, *68*, 4369–4380. [[CrossRef](#)]
14. Guo, F.; Xia, L.; Yang, T.; Xu, R. A Novel Metamaterial Transmission Line with Adjustable Left-Handed Elements and Its Application to H-plane Filter. *IEEE Microw. Wirel. Compon. Lett.* **2018**, *28*, 774–776. [[CrossRef](#)]
15. Pirrone, D.; Ferraro, A.; Zografopoulos, D.C.; Fuscaldo, W.; Szriftgiser, P.; Ducournau, G.; Beccherelli, R. Metasurface-based filters for high data rate THz wireless communication: Experimental validation of a 14 Gbps OOK and 104 Gbps QAM-16 wireless link in the 300 GHz band. *IEEE Trans. Wirel. Commun.* **2022**, *21*, 8688–8697. [[CrossRef](#)]
16. Liu, H.; Wen, P.; Jiang, H.; He, Y. Wideband and low-loss high-temperature superconducting bandpass filter based on metamaterial stepped-impedance resonator. *IEEE Trans. Appl. Supercond.* **2016**, *26*, 1500404. [[CrossRef](#)]
17. Jyothi, M.H.; Bipin, D.V.; Choudhury, B.; Nair, R.U. Design of conformal metamaterial unit cells for invisibility cloaking applications. In Proceedings of the 2016 IEEE Annual India Conference (INDICON), Bangalore, India, 16–8 December 2016; pp. 1–5.
18. Takano, Y.; Sanada, A. Polarization independent isotropic near-zero-index metamaterials composed of dielectric spheres for 3-D invisibility cloaks. In Proceedings of the 2017 IEEE Asia Pacific Microwave Conference (APMC), Kuala Lumpur, Malaysia, 13–16 November 2017; pp. 345–348.
19. Ramaccia, D.; Souнас, D.; Alu, A.; Toscano, A.; Bilotti, F. Advancements in doppler cloak technology: Manipulation of doppler effect and invisibility for moving objects. In Proceedings of the 10th International Congress on Advanced Electromagnetic Materials in Microwaves and Optics (METAMATERIALS), Crete, Greece, 17–22 September 2016; pp. 295–297.
20. Wang, X.; Chen, F.; Semouchkina, E. Implementation of low scattering microwave cloaking by all-dielectric metamaterials. *IEEE Microw. Wirel. Compon. Lett.* **2013**, *23*, 63–65. [[CrossRef](#)]
21. Chirala, M.K.; Floyd, B.A. Millimeter-wave Lange and ring-hybrid couplers in a silicon technology for E-band applications. In Proceedings of the IEEE MTT-S International Microwave Symposium Digest, San Francisco, CA, USA, 11–16 June 2006; pp. 1547–1550.
22. Ding, H.; Lam, K.; Wang, G.; Woods, W.H. On-chip millimeter wave rat-race hybrid and Marchand balun in IBM 0.13 μm BiCMOS technology. In Proceedings of the Asia-Pacific Microwave Conference, Hong Kong, China, 16–20 December 2008; pp. 1–4.
23. Chirala, M.K.; Nguyen, C. Multilayer design techniques for extremely miniaturized CMOS microwave and millimeter-wave distributed passive circuits. *IEEE Trans. Microw. Theory Techn.* **2006**, *54*, 4218–4224. [[CrossRef](#)]
24. Ng, C.Y.; Chongcheawchamnan, M.; Robertson, I.D. Miniature 38 GHz couplers and baluns using multilayer GaAs MMIC technology. In Proceedings of the 33rd European Microwave Conference Proceedings, Munich, Germany, 7–9 October 2003; Volume 3, pp. 1435–1438.
25. Garay, E.; Huang, M.-Y.; Wang, H. A cascaded self-similar rat-race hybrid coupler architecture and its compact fully integrated Ka-band implementation. In Proceedings of the IEEE/MTT-S International Microwave Symposium-IMS, Philadelphia, PA, USA, 10–15 June 2018; pp. 79–82.
26. Huang, M.-Y.; Wang, H. An ultra-compact folded inductor based mm-wave rat-race coupler in CMOS. In Proceedings of the IEEE MTT-S International Microwave Symposium, San Francisco, CA, USA, 22–27 May 2016; pp. 1–4.
27. Lin, Y.-S.; Lu, P.-S.; Lu, C.-Y. Miniature V-band rat-race coupler in CMOS using cascaded bridged-T coils. *IEEE Trans. Microw. Theory Tech.* **2023**, *71*, 737–749. [[CrossRef](#)]
28. Lin, I.-H.; de Vincentis, M.; Caloz, C.; Itoh, T. Arbitrary dual-band components using composite right/left-handed transmission lines. *IEEE Trans. Microw. Theory Tech.* **2004**, *52*, 1142–1149. [[CrossRef](#)]
29. Mao, S.-G.; Chen, S.-L.; Huang, C.-W. Effective electromagnetic parameters of novel distributed left-handed microstrip lines. *IEEE Trans. Microw. Theory Techn.* **2005**, *53*, 1515–1521.
30. Caloz, C.; Itoh, T. Transmission line approach of left-handed (LH) materials and microstrip implementation of an artificial LH transmission line. *IEEE Trans. Antennas Propag.* **2004**, *52*, 1159–1166. [[CrossRef](#)]

Disclaimer/Publisher’s Note: The statements, opinions and data contained in all publications are solely those of the individual author(s) and contributor(s) and not of MDPI and/or the editor(s). MDPI and/or the editor(s) disclaim responsibility for any injury to people or property resulting from any ideas, methods, instructions or products referred to in the content.